TRAPPED NON-WETTING PHASE CLUSTERS: AN EXPERIMENTAL INVESTIGATION OF DYNAMIC EFFECTS AT THE PORE SCALE USING A MICRO-CT SCANNER

M. Khishvand, M. Akbarabadi, M. Piri

Chemical and Petroleum engineering department, University of Wyoming, Laramie, Wyoming, USA

ABSTRACT

We used a state-of-the-art micro-CT scanner integrated with a two-phase core-flooding apparatus to perform flow experiments in a Bentheimer sandstone core sample in order to investigate the impact of dynamic effects on the trapping of non-wetting (oil) phase at the pore scale. We explore the size distribution of the trapped oil clusters at the pore level. The sample was 4.9 mm in diameter and 13 mm long. A new core holder was designed and built to allow flow experiments through small core samples (under confining pressure) while located inside the micro-CT scanner. An unsteady-state method was utilized to carry out three sets of experiments on the sample; each set included a drainage and imbibition cycle with identical initial brine saturation (i.e., $S_{wi}=0.34$) prior to each imbibition step. During imbibition, different brine flow rates were used to create flows with various capillary numbers, ranging from 10^{-6} to about 10^{-5}, to cover both capillary-dominated and viscous-dominated displacement regimes. The pressure and temperature of the experiments were 24 °C and 2.76 MPa, respectively. We mapped fluid occupancies at the end of each drainage and imbibition step for the entire sample. The S_{or} decreased significantly from 0.41 to 0.16 during the imbibition processes due to stronger viscous pressure drop at the end of the third imbibition compared to those of the first two imbibition tests. The contact area between oil and brine was considerably decreased at the end of the high imbibition brine flow rate compared to those of the first and second imbibition tests.

INTRODUCTION

Multiphase flow and transport in porous media and characterization of the associated phenomena are of great interest in science and engineering. Enhanced hydrocarbon recovery, CO_2 sequestration in geologic formations, and aquifer contaminant remediation are some of the major applications. In order to predict the performance of reservoir-scale flow schemes, one often needs to use reservoir simulators designed to solve mass conservation equations numerically. These simulators read as input multiphase flow functions such as relative permeabilities that are either measured or predicted by physically-based pore-scale models, e.g., pore network and direct models. These

experiments are usually expensive and time consuming. Therefore, there have been numerous investigations to develop pore-scale models with improved predictive capabilities [1-4]. These models use as input a faithful representation of the pore space (e.g., a random pore network) and simulate relevant displacement mechanisms to predict multiphase flow functions taking into account hysteresis and wettability effects. X-ray micro-computed tomography (μ-CT) can be used to provide not only accurate maps of the pore space (used to construct the pore networks) but also other information (e.g., fluid occupancy, interfacial area, etc.) to validate the above-mentioned models.

Characterizing the fluid occupancy accurately during core-flooding experiments and investigating the impact of the capillary- and viscous-dominated displacement regimes can prove very valuable in rigorous validation of pore-scale models and hence improving their predictive capabilities. Over the last decade, growing number of studies have been presented in the literature that are focused on this specific area of research [5-16]. Karpyn et al. [9] used a μ-CT scanner to investigate the distribution and configuration of the trapped oil clusters under different flow conditions (drainage and imbibition) in a water-wet glass bead pack. The voxel resolution was 0.026000mm×0.026000mm×0.029205 mm. They reported that the residual oil saturation was very low, i.e., 17.7%, which was attributed to the good hydraulic conductivity of the oil phase and gravity segregation. Silin et al. [10] studied the spatial distribution of the fluids in the pore space of a Frio sandstone core sample with 5.5 mm diameter and 20.16 mm length using a Synchrotron-based imaging system. They also characterized the capillary pressure curve of the medium. The voxel resolution of the data was 4.48 μm. To calculate the capillary pressure through application of Young-Laplace equation, they used the Maximal Inscribed Spheres (MIS) technique in which a sphere with the radius of R was inscribed in the interface between the wetting and non-wetting phases. Krummel et al. [14] explored the effect of capillary number on the formation of the trapped oil clusters during the imbibition process using a μ-CT scanner. They performed the flow experiments in a water-wet glass bead pack. The beads had an average radius of 32 to 75 μm. They were placed in a series of rectangular quartz capillaries with thin walls. They observed thin layers of the wetting phase on the surfaces, which caused the trapping of the non-wetting phase through snap-off. They reported that when the capillary number increased, the trapping caused by snap-off decreased. They reported that the viscous forces mobilized the oil clusters.

In this paper we use a state-of-the-art μ-CT scanner integrated with a two-phase flow core-flooding apparatus to investigate the impact of the dynamic effects, corresponding to high capillary number flow regimes, on the trapped oil clusters during imbibition. We study the size, shape, and distribution of the oil globules during the drainage and imbibition experiments.

MATERIALS AND EXPERIMENTAL METHODOLOGY

In this section, we explain the properties of the core sample and fluids, experimental conditions, setup, and procedures used in this study.

Three sets of unsteady-state drainage-imbibition flow experiments were performed in a Bentheimer sandstone (SS) core. The sample was 4.9 mm in diameter and 13 mm long. Petrophysical properties of the core are summarized in Table 1. In this study, we used n-Decane as the non-wetting phase and brine with 1.5 wt% NaI as the wetting phase. The experiments were carried out at ambient temperature, i.e., 24 °C, and 2.76 MPa back pressure. The overburden pressure was maintained at 4.83 MPa. The physical properties of the fluids under the above-mentioned conditions are listed in Table 2. Three experiments were carried out to investigate the impact of dynamic effects on the trapped oil clusters and residual saturation during the imbibition. The experiments were performed at different capillary numbers to establish different displacement regimes. The experimental setup is a two-phase, reservoir-conditions core-flooding apparatus, which includes four dual-cylinder 5000-series Quizix pumps, a Versa XRM 500 µ-CT scanner, a micro core holder, a pressure array system to measure the pressure drop along the core, and a data acquisition and control system. We designed and built the micro core holder that allows us to perform two- and three-phase flow experiments in small core samples (e.g., 3-10 mm diameter) while under confining pressure. A schematic flow diagram of the apparatus is illustrated in figure 1. P1, P2, P3, and P4 are brine, oil, back pressure regulation (BPR), and overburden pressure pumps, respectively. P1 and P2 retract brine and oil from two separate containers and inject them into the bottom of the core holder with constant flow rate, whereas P3 retracts the effluent mixture from the top of the core holder at constant back pressure. The process was implemented using an open-loop approach. P3 allowed us to establish a noticeably stable outlet pressure. This was essential as fluctuations in the back pressure would change the pore fluid configurations during drainage and imbibition tests. P4 was used to maintain a constant radial overburden pressure using Nitrogen as the overburden fluid. The main body of the core holder was made out of Aluminum. It included two Titanium nozzles and one thin Viton sleeve. The diameter and the length of the core holder were 12 mm and 11.43 cm, respectively. The pressure array included four Rosemount pressure transducers with various ranges for differential pressure.

The X-ray equipment operates through obtaining projections of the sample, which is rotated on a stage while the detector and source are fixed in predetermined positions. The detector objectives and the x-ray source can be moved along the Z-axis to enable geometrical magnification. The detector comprises an ANDRO camera and six objectives (i.e., 0.4X, 1X, 4X, 10X, 20X, and 40X) that allow objective magnification. When these two techniques are used together, the scanner can produce resolutions as high as 500 nm. The X-ray source can generate 30 to 160 KV voltages and 1 to 10 W powers. The tomographies are re-constructed and processed using *XM-Reconstructor* of *X-radia* to produce high-quality images.

After installing the core holder and core sample in the µ-CT scanner, the core was flushed with dry CO_2 and then vacuumed to remove trapped air from the sample and the flow lines. The entire length of the core was scanned to attain the dry scan, which was used for accurately mapping the saturation distribution of the fluid phases and porosity distribution along the length of the core. It was then subjected to brine injection to

produce a brine-saturated core. At the end of this stage, the core was imaged to acquire another reference scan. At this point, we started the drainage test followed by imbibition. Oil was injected into the core with the flow rate of 0.005 cc/min using P2. We gradually increased the flow rate to 0.03 cc/min and continued to inject oil for about 10 hours. During the drainage, we monitored the pressure drop and scanned the core frequently at lower resolutions (3.6 μm, monitoring scans) until the steady state was reached. This is when the oil saturation did not change and the pressure drop was constant. At this point, the entire length of the core was imaged (at 2.6 μm resolution) to determine initial brine saturation (S_{wi}) using an automated stitching method. We also imaged the middle section (2 mm * 2 mm) of the core at a higher resolution (2.0 μm) at the end of each drainage and imbibition process. After determining the initial brine saturation, the imbibition process was initiated through injection of brine at a low flow rate. Similar to the drainage test, we monitored the saturation in the core and recorded the pressure drop until the steady state was established. When slight increase in brine flow rate did not change the saturation profile in the core, imbibition was considered complete. The core was imaged using the auto-stitching method to obtain residual oil saturation. This was then followed by a high-resolution scan of the middle section of the core. Prior to starting the second imbibition with higher flow rate, a secondary oil drainage process was initiated (with maximum flow rate of 0.03 cc/min) to establish the same initial brine saturation as the onset of the first imbibition. A protocol similar to the one used for the first drainage-imbibition cycle was followed during the second and third cycles with this difference that imbibition brine flow rate was increased 5 and 50 fold for the second and third imbibition tests, respectively. The appropriate brine flow rates, corresponding to the pre-specified capillary numbers (N_c), were calculated using the following equation:

$$N_c = \frac{\mu_w \times u_w}{\varphi \times \sigma_{ow}} \qquad (1)$$

where μ_w, u_w, φ, and σ_{ow} are brine viscosity, brine velocity, porosity, and oil/brine interfacial tension, respectively. In table 3, the experiments with the corresponding maximum brine flow rates (Q_w^{max}), capillary numbers, and the initial brine and ultimate residual oil saturations are listed.

Data acquisition

After mounting the core holder on the stage in the μ-CT scanner, the optimum parameters for different imaging conditions were selected and stored in a recipe for frequent use. Each recipe included: optimum source kV, source power, objective selection, binning selection, tomography locations, exposure time, number of projections, and source and detector positions to obtain desired resolution and field of view without any collision of the core holder, source, and detector during specimen rotation. The parameters for monitoring, auto stitching, and high-resolution scans were different from each other and were saved as separate recipes (see table 4). Once each recipe was executed, the sample rotation was initiated and tomography projections of the objective were generated, captured using an ANDRO camera, and saved on a computer. The projections and the sample drift were saved as two separate stacked files. Sample drift data set was used

during re-construction to reduce the artifact on the re-constructed slices. The next step was data re-construction during which the data was loaded using *XM-Reconstructer* software to attain the center shift, perform beam hardening, and produce stacked two-dimensional slices. Each data set was re-constructed by applying: shift, beam hardening, defect correction, ring removal, secondary referencing, global minimum and maximum, and Kernel smoothing. Determining and applying center shift, which represents the distance between central axis of sample rotation and central column of the detector, was the most important part of the data re-construction process. Global minimum and maximum were used to make close intensity value of each phase for different data sets in imbibition or drainage. Secondary referencing and re-construction ring removal were two powerful methods used to remove ring diffuse in the images. Finally, kernel smoothing of 0.8 (in all cases) was carried out to increase signal to noise ratio. In a stitched scan, three sets of scans were re-constructed separately and stitched vertically with a 25 % overlap in the Z-axis. This data set includes 5071 slices, which were used for saturation calculations after they were processed using AvizoFire software. In this paper we present the data from only the middle set.

DATA PROCESSING

In this step, we used different modules of AvizoFire software to generate quantitative results from the raw data exported from the μ-CT scanner. Analyzing the data comprised three different steps: pre-processing, subtraction and segmentation, and quantification. Using these steps along with a subtraction method allowed us to generate high-quality segmented data.

The first step in pre-processing was data filtering. The images obtained from the μ-CT scanner contained noises generated by artifacts. These noises can create undesired issues during the segmentation process such as phase mixing in which the fluid phases cannot be segmented properly. Therefore, various types of filtering and smoothening processes were applied among which the non-local mean filter produced the best result. As the sample in the core holder had a very small inclination from the vertical axis, a new method was applied to rotate all the slices. Prior to starting the segmentation process, we employed the volume edit module on the filtered file to exclude slices related to the sleeve and the edges of the sample. The result of this procedure is referred to as the "masked-filtered" data throughout the text.

Instead of implementing the common segmentation procedure in which the reference images are used to register the data, we applied the following protocol to create a high-quality segmented file for the quantification step: 1) the masked-filtered data was divided using oil intensity, which was obtained utilizing the point probe module, 2) a binary file was created from the output of the step 1 in which the pores were assigned as 1 and the grains as 0, 3) the output of the step 2 was subtracted from the results of item 1, and 4) the "watershed" segmentation module was applied to segment the result. To perform the segmentation (step 4), a range of threshold values was defined using intensity histogram with 256 bins for each phase present in the core sample, i.e., brine, oil, grains, and the

exterior phases. At this point, we used the quantification module to analyze the segmented data in order to calculate the saturations and other parameters.

Quantification is a method by which we can calculate the saturation of each phase, clusters size and volume, and interfacial area. In this study, we used different quantification tool options such as i-analyze in AvizoFire to evaluate the binary data obtained from the segmentation process.

RESULTS AND DISCUSSIONS

In this section, we present the results of the drainage and imbibition core-flooding experiments. We study the impact of the dynamic effects on the trapped oil clusters formed by imbibition.

Drainage

During the drainage step in all three cycles, oil was initially injected into the sample with the low flow rate of 0.005 cc/min; the flow rate was then gradually increased to a maximum of 0.03 cc/min to establish the initial brine saturation for the subsequent imbibition process. Table 3 lists the initial brine saturation at the end of three drainage tests. The results show that the S_{wi} was similar, i.e., 0.34, in all three cycles.

Imbibition

At the end of each drainage step, we initiated the imbibition test to reach a pre-specified maximum brine flow rate (see table 3). After reaching the residual oil saturation, we imaged the entire length of the core sample (three compartments) at 2.6 μm resolution followed by a higher resolution (2.0 μm) scan of the middle section of the core (see table 4). The average oil saturation of the middle compartment at the end of the first and second imbibition tests were 0.41 and 0.37, respectively, while it was 0.16 at the end of the third imbibition. This decrease is due to significant pressure drop along the core. During the third imbibition, displacement of oil-filled pores by brine is significantly affected by viscous pressure drop relevant to each displacement [17]. Note that the initial brine saturation for all three imbibition experiments was identical. Figure 2 shows two-dimensional segmented images of oil and brine distribution at two locations along the length of the core and also three-dimensional saturation distribution for the middle section of the core for drainage and the second and third imbibition tests. Figure 3 presents three-dimensional visualization of the first three largest oil globules distribution at the end of the second and third imbibition tests. It shows that the trapped oil clusters were reduced in size significantly due to stronger viscous forces during the third imbibition experiment. Figure 4 shows the frequency of each oil blob volume group at the end of all imbibition cycles. To generate this histogram, we categorized the volume of isolated oil blobs into several groups and sub-groups, and determined the frequency in each sub-group. It is evident that the frequency in groups with large globules has reduced. Furthermore, a significant increase is observed in the frequency of the group with smallest oil blobs. Figure 5 illustrates cumulative volume of trapped oil versus blob volume. The position of the third imbibition curve is distinctly different from those of the first and second imbibition tests. The sharp increase in cumulative volume is observed

over much smaller blob volumes (0.0001 to 0.01) while that is 0.001 to 0.1 for the first two imbibition tests. These ranges cover approximately 55% and 40% of the total residual oil in the sample, respectively. In all cases, the contribution of the blobs with large volume, e.g., larger than 0.2, to the trapped oil is insignificant. In Figure 6, the distribution of the trapped oil clusters with various sizes along the length of the core (middle compartment) for two imbibition cycles are presented. In this graph, each point represents the geometric center of the individual oil globules. The clusters of the third imbibition are concentrated over a shorter range of blob volume (with smaller globules) while those of the first imbibition test are more spread out (with larger globules). Figure 7 shows the distribution of the oil blob lengths along the middle compartment of the core sample for the first and third imbibition tests. As it is seen, the clusters of the third imbibition are shorter as well as having smaller volumes. Figure 8 depicts the blob aspect ratio. This figure indicates that the blob aspect ratios in the third imbibition are less scattered than those of the first imbibition. The results show slightly different trend compared to those obtained from the experiments performed on glass bead packs [9], where the blob aspect ratios were closer to 1. This might be due to the fact that the pore size distribution in the glass bead pack is significantly different than that of the rock sample used in this study. In figure 9A, oil clusters' surface area is presented with respect to the cluster volume. This figure shows that the large volume clusters expectedly have higher surface area. The trend is very similar for the first and third imbibitions processes. The difference between two imbibition tests can be observed at two ends of the blob volume spectrum. For the third imbibition, significant amount of the very large oil clusters are absent. This phenomenon was also shown in figures 6 and 7. The surface area to volume ratio for both imbibition cycles is exhibited in figure 9B. It can be seen that by increasing the volume of the clusters, the surface area to volume ratio decreases until the blob volume of .01 mm^3 beyond which the ratio reaches to a plateau of about 50 mm^{-1}. Figure 10 shows the contact area between oil/brine and brine/grain at the end of the second and third imbibition tests. In this figure, it is evident that the contact area between oil/brine at the end of the third imbibition was noticeably decreased while the brine/grain contact area was increased. This is consistent with the fact that the oil clusters formed during the third imbibition were smaller with lower overall trapped oil saturation. In other words, more pores were saturated with brine.

CONCLUSIONS

We performed three unsteady-state, drainage-imbibition flow experiments on a Bentheimer SS core sample (D= 4.9 mm, L=13 mm) using a state-of-the-art X-ray μ-CT scanner integrated with a two-phase core-flooding apparatus. We investigated the impact of the dynamic effects on the shape, size distribution, and configuration of the non-wetting phase clusters, i.e., oil, at the pore level and also on the trapping of the oil. During the flow experiments, we used drainage step to generate the same initial brine saturation for the subsequent imbibition tests. Two imbibition tests were carried out under capillary-dominated displacement regime while the third imbibition test was performed at a much higher flow rate. The maximum flow rates for the first, second, and

third imbibition tests were 0.015, 0.075, and 0.75 cc/min, respectively. We processed the images using various modules of AvizoFire software in order to remove any artifacts. This was then followed by the quantification process to calculate oil saturation and blob volume and size distribution. We found that the residual oil saturation at the end of the imbibition processes varied from 0.41 to 0.16. The results showed that the trapped oil saturation significantly decreased at the end of the third imbibition compared to those of the first two tests due to stronger viscous pressure drop across the core sample. We scanned the entire length of the core sample, and observed that the oil globules were significantly smaller due to the dynamic effects. The oil cluster aspect ratios obtained during this study were slightly different from those of the glass bead pack reported in the literature, in that, the shape of the oil blobs in the latter was more spherical. The contact area between oil and brine was significantly decreased at the end of the last imbibition compared to that of the first imbibition due to significantly reduced residual oil saturation and oil globule sizes.

ACKNOWLEDGMETS

REFRENCES

1. P.E. Øren, S. Bakke, and O.J. Arntzen. Extending predictive capabilities to network models, SPE J., (1998) 3(4), 324–336.
2. Mark A. Knackstedt, Adrian P. Sheppard, Muhammad Sahimi. Pore network modeling of two-phase flow in porous rock: the effect of correlated heterogeneity, Adv. Water Resour, (2001) 24,257-277.
3. M. Piri and M. J. Blunt. Three-dimensional mixed-wet random pore-scale network modeling of two- and three-phase flow in porous media. I. Model description, Phys. Rev. E, 71, 026301, (2005a) doi:10.1103/PhysRevE.71.026301.
4. M. Piri and M. J. Blunt Three-dimensional mixed-wet random pore-scale network modeling of two- and three-phase flow in porous media. II. Results. Phys. Rev. E, 71, 026302, (2005b) doi:10.1103/PhysRevE. 71.026302.
5. Z.T. Karpyn, A.S. Grader, P.M. Halleck. Visualization of fluid occupancy in a rough fracture using micro-tomography. J. Colloid Interface Sci. 307 (2007) 181–187.
6. Z.T. Karpyn and M. Piri. Prediction of fluid occupancy in fractures using network modeling and X-ray micro tomography. Part 1: Data conditioning and model description, Phys. Rev. E, (2007) 76, 016315, doi:10.1103/PhysRevE.76.016315.
7. M. Piri and Z. T. Karpyn. Prediction of fluid occupancy in fractures using network modeling and X-ray micro tomography. Part 2: Results, Phys. Rev. E, (2007) 76, 016316, doi:10.1103/PhysRevE.76.016316.
8. Y. S. Yang, T E Gureyev, A. Tulloh, M B Clennell and M Pervukhina. Feasibility of a data-constrained prediction of hydrocarbon reservoir sandstone microstructures. Meas Sci Technol (2010) 21(4).
9. Z.T. Karpyn, M. Piri, Singh G. Experimental investigation of trapped oil clusters in a water-wet bead pack using X-ray micro tomography. Water Resour Res (2010) 46(4).
10. D. Silin, L. Tomutsa, S. M. Benson. Microtomography and pore-scale modeling of two-phase fluid distribution. Transp Porous Media (2011) 86(2):495–515.
11. Landry CJ, Karpyn ZT, Piri M. Pore-scale analysis of trapped immiscible fluid structures and fluid interfacial areas in oil-wet and water-wet bead packs. Geofluids (2011) 11(2):209–27.

12. R.T. Armstrong, M.L. Porter, D. Wildenschild. Linking pore-scale interfacial curvature to column-scale capillary pressure. Adv Water Resour (2012) 46:55–62.
13. D. Wildenschild, A.P. Sheppard. X-ray imaging and analysis techniques for quantifying pore-scale structure and processes in subsurface porous medium systems. Advances in Water Resources, (2013) 51,217-246.
14. Amber T. Krummel, Sujit S. Datta, Stefan Münster, David A. Weitz, Visualizing Multiphase Flow and Trapped Fluid Configurations in a Model Three-Dimensional Porous Medium, AIChE Journal, (2013) 59(3),1022-1029.
15. A. L. Lee, R. T. Ellington. Viscosity of n-Decane in the liquid phase. Journal of Chemical and Engineering Data (1965) 10(4), 346-348.
16. Susana Zeppieri, Jhosgre Rodriguez, and A. L. Lopez de Ramos. Interfacial Tension of Alkane Water Systems. J. Chem. Eng. Data (2001) 46, 1086-1088.
17. M. Akbarabadi, M. Piri. An Experimental Study of Capillary Trapping, Relative Permeability, and Capillary pressure of $scCO_2+SO_2$/brine/limestone system. To be submitted.

Table 1.Dimensions and petrophysical properties of the Bentheimer core sample used in this study.

Core	Length (mm)	Diameter (mm)	φ (X-ray)	k_{abs} (brine) mD	PV (cm^3)
Bentheimer	13	4.90	0.238	2572	0.0576

Table 2. Physical properties of the fluids used in this study [15,16].

Fluids	Density (kg/m^3)	Viscosity (cP)	Oil/brine IFT (mN/m)
Decane	735.4	0.8345	51.7
Brine	1009	0.92	

Table 3. Number of experiments, the maximum imbibition brine flow rates, and their corresponding capillary numbers.

Exp. No.	Process	Q_w^{max} (cm^3/min)	Capillary number (N_c)	S_{wi}	S_{or}
1	Drainage-imbibition	0.015	1.07×10^{-6}	0.34	0.41
2	Drainage-imbibition	0.075	5.34×10^{-6}	0.34	0.37
3	Drainage-imbibition	0.75	5.34×10^{-5}	0.34	0.16

Table 4. The parameters used with different recipes during X-ray imaging.

Recipe type	D (mm)	L (mm)	No. of projections	Voxel res. μm (x,y,z)	Exposure time (s)	Camera Binning*	Field of view	Scan duration (hr)
Monitoring scans	3.6	3.6	3000	3.6,3.6,3.6	0.5	2	4X	2
Auto stitching	5.2	13	3*4500	2.6,2.6,2.6	5.5	1	4X	3*8
High resolution	2	2	6000	2.0,2.0,2.0	1.8	2	4X	5

*: This parameter is used to obtain a higher quality image with smaller field of view. The higher the value, the smaller the field of view, and finally, the better image quality without changing the exposure time.

Figure 1. Schematic of the core-flooding setup used in this study.

Figure 2. 2D and 3D Oil and brine distribution in Bentheimer SS at different locations from inlet and at different flow conditions (red: grain, yellow: brine, dark blue: oil, Resolution: 2 μm)

Process (size order)	2nd imb. (1)	2nd imb. (2)	2nd imb. (3)	3rd imb. (1)	3rd imb. (2)	3rd imb. (3)
First three largest oil blobs						
Size (mm³)	0.336698	0.223369	0.198633	0.03606	0.03523	0.02759
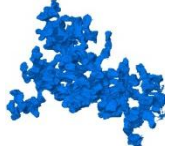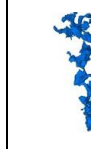
Figure 3. 3D visualization of the first three largest oil clusters at the middle section of the core at the end of the second and third imbibition tests.
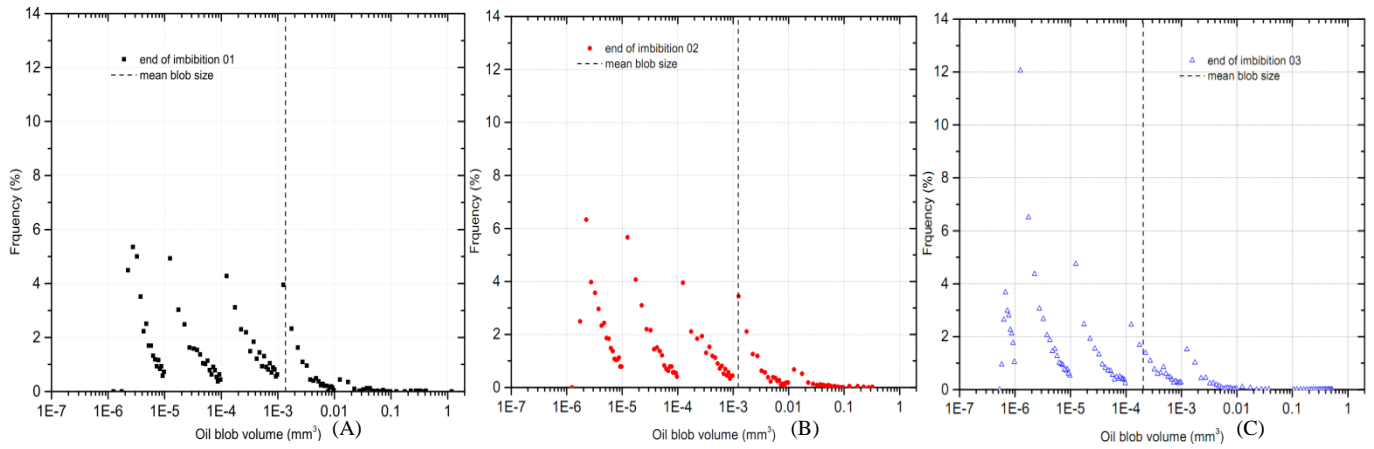
Figure 4. Frequency of different groups of oil blob volume at the end of A) first, B) second, and C) third imbibition tests.
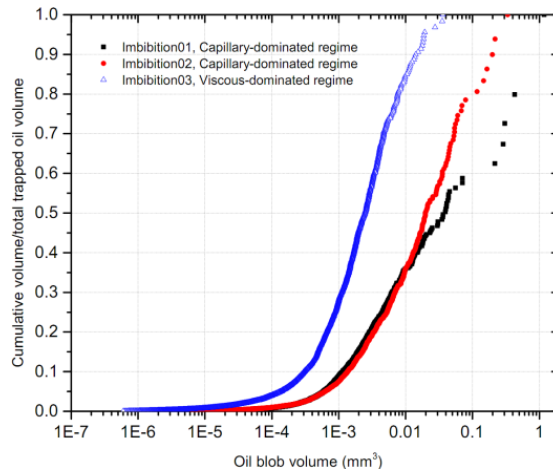
Figure 5. The ratio of cumulative to total trapped oil volume versus oil blob volume at the end of the three
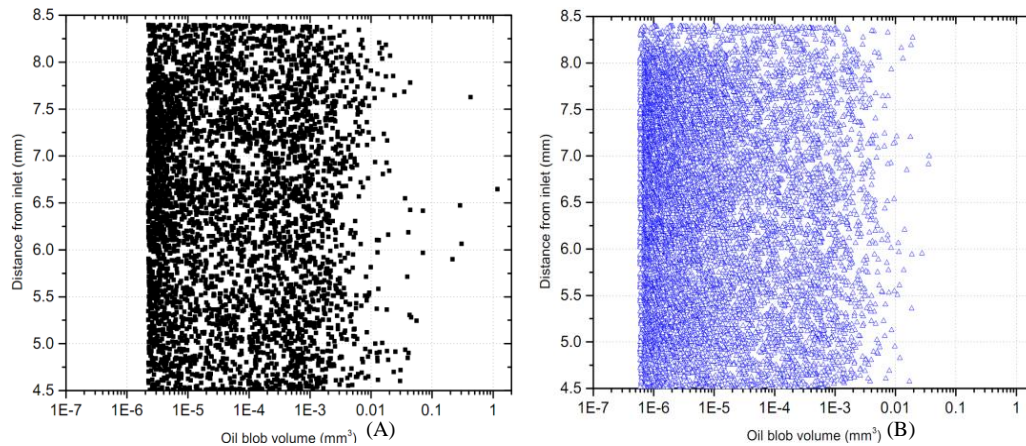
imbibition tests.
Figure 6. Spatial distribution of oil blob volume along the length of the sample at the end of A) first and B) third imbibition tests.

Figure 7. Distribution of maximum blob length along the length of the core sample at end of A) first and B) third imbibition tests. Different colors represent different blob volumes.
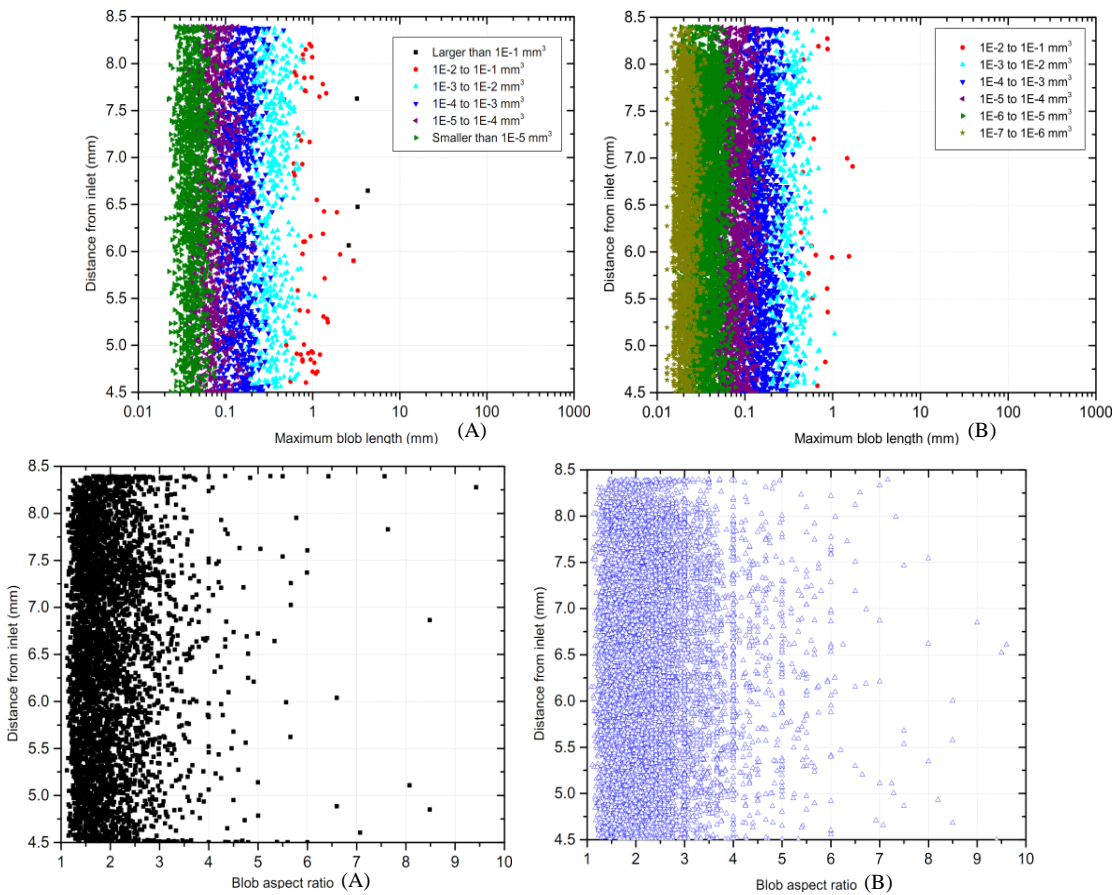
Figure 8. Blob aspect ratio along the length of the core sample at the end of A) first and B) third imbibition tests.
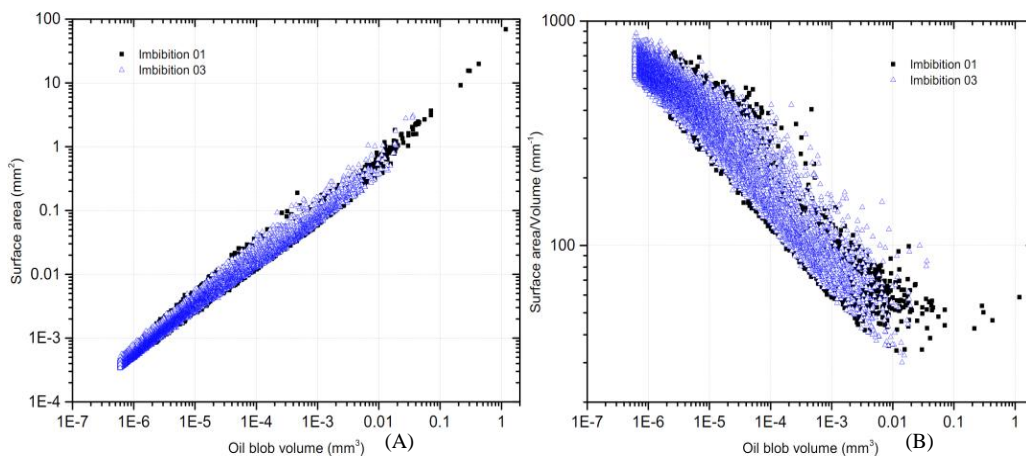
Figure 9. Variation of A) oil bob surface area and B) surface area-to-volume ratio with oil blob volume at the end of first and third imbibition tests.
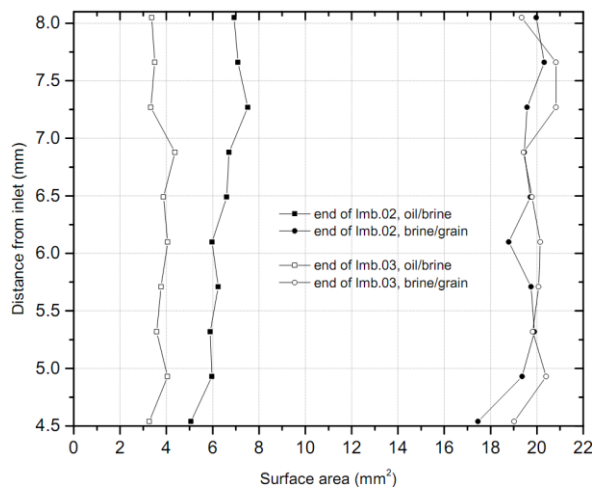
Figure 10. Surface areas along the length of the core sample at the end of the first and last imbibition tests.